MINISTRY OF EDUCATION AND SCIENCE IN UKRAINE
Taras Shevchenko National University of Kyiv
Physics faculty
Nuclear physics department

on the rights of the manuscript

Development of the LumiCal detector for the ILC project

Discipline: 10 Natural sciences
Specialty: 104 Physics and astronomy
Educational program: High energy physics

Qualifying work of the master
of 2nd year student
Dudar Bohdan Viktorovich
Scientific advisor:
prof. Halina Abramowicz
Curator of the department:
doctor of phys. and math., Assoc.
Aushev Volodymyr Egorovich

This document is a translation of the master thesis submitted to the Taras Shevchenko National University of Kyiv.

Kyiv — 2020

SUMMARY

Dudar B.V. Development of LumiCal detector for ILC project.

Masters qualification work in specialty 104 Physics and astronomy, educational program ”High energy physics”. — Taras Shevchenko National University of Kyiv, Faculty of Physics, Department of Nuclear Physics. — Kyiv — 2020.

Research supervisor: Professor of Physics Halina Abramowicz, prof. of School of Physics and Astronomy of Tel Aviv University.

Curator from the department: Dr. of Physics and Mathematics, Associate Professor Aushev V.E., Associate Professor of Department of Nuclear Physics.

Test beam of LumiCal calorimeter with two tracker planes in front at DESY in 2016 with 5 GeV electrons was simulated in Geant4 software. Algorithm for reconstruction of number of showers and their position in the calorimeter was written. Quantity and nature of back scattering from calorimeter that is registered by tracker were studied. Impact of back scattering on shower inducing particles identification algorithm was studied. Participated in test beam of LumiCal in March 2020.

Key words: calorimeter, LumiCal, identification, back scattering, test beam.

Contents

Introduction

This work involved the development of a detector for a future ILC project aimed at finding new physics outside the Standard Model.

The LumiCal detector under study has two functions within the ILC detector system. The first — accurate measurement of luminosity. The second" — the potential introduction of particle identification at small angles of spread.

The identification of LumiCal particles by the detector strongly depends on the spurious signals in the front sensors located in front of the calorimeter. One of the sources of spurious signals in the sensors is the backscattered particles from the calorimeter. If the contribution of signals from the backscattered particles is sufficient, this may make particle identification impossible, which will complicate the reconstruction of events and reduce the accuracy of measurements on the ILC.

This study investigated the effect of backscattering from a LumiCal calorimeter on particle identification, which is necessary, for example, to accurately measure the cross section of liquid reactions on ILC.

Data from LumiCal calorimeter tests in 2016 on the DESY-II accelerator were used and this data was simulated in Geant4.

The prototype of the detector with the location of two Si sensors in front of the calorimeter as a tracker for the introduction of particle identification was investigated.

Also in collaboration with the FCAL collaboration, the author participated in testing of the LumiCal detector in March 2020. The paper provides information about new measurements and updates of the LumiCal prototype.

1 Overview

1.1 Standard Model

The standard model (SM) is a theory that was developed in the 1970s to describe all observed elementary particles and their interactions.

The discovery of the Higgs boson in 2012 at the LHC (Large Hadron Collider) [1] was the final confirmation of this model and it still remains the most popular for describing particle physics.

But SM is not the ultimate model of our world, as it cannot explain a number of observed phenomena [2]. Such as:

- Asymmetry of baryon matter in the universe
- Gravity
- Neutrino oscillations
- Dark matter, dark energy
- Anomalous magnetic moment of a muon, etc.

To improve our understanding of the universe and explain the differences between experiments with SM, many different projects have been proposed that measure interactions with higher accuracy than at the LHC and new parameter areas that have not yet been measured due to technological limitations.

One of the proposed projects that can explain the differences between CM and modern experiments is the ILC project (International Linear Collider) [3].

1.2 ILC

ILC is a linear e^+e^- collider with an energy in the center of mass of 250 GeV with a possible increase to 1 TeV and integrated luminosity for the first four years of operation 400 fbn $^{-1}$.

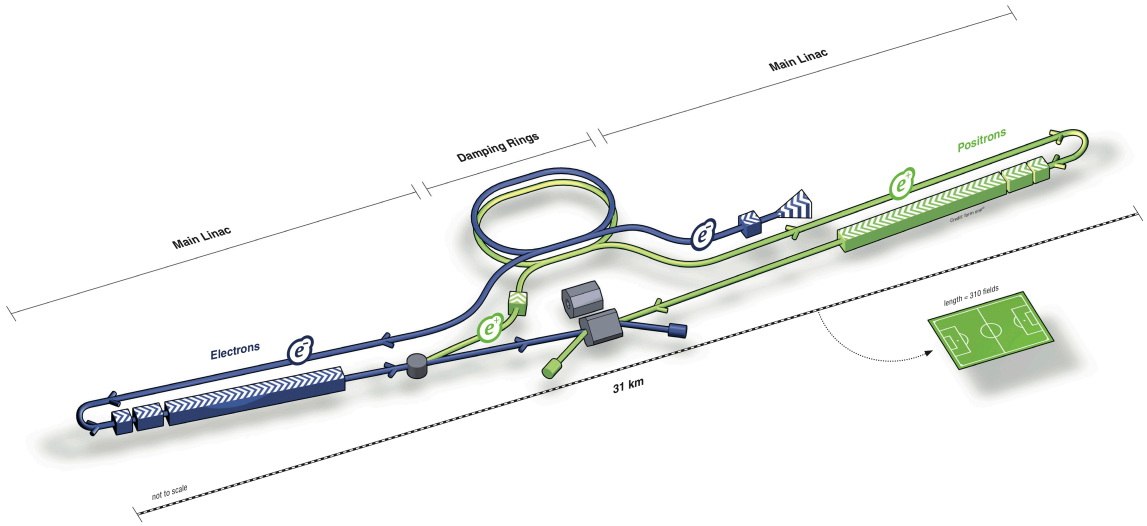

Figure 1.1: ILC schematic.

One of the purposes of ILC is to accurately measure the cross sections of the reactions of elementary particles.

The cross section of reactions is measured by recording events with this reaction for a certain period of time, which is expressed by the luminosity parameter. Then the cross section can be found by the formula: $\sigma = \frac{N_{events}}{L}$, where σ is the cross section of a certain reaction, N_{events} is the number of detected events with this reaction, L - integrated luminosity for a certain period of time.

It is important that the accuracy of the reaction cross sections depends on the accuracy of the luminosity measurement and the correct reconstruction of the events.

For ILC, there are several options for building a system of detectors: ILD (International Linear Detector) and SiD (Silicon Detector) [3; 4].

Both variants have a calorimeter in the design of the front area of the detector system, called LumiCal (Luminosity Calorimeter) [4; 5]. It is designed to measure luminosity with an accuracy of $\frac{\Delta L}{L} = 10^{-3}$ [6] and to introduce particle identification at polar angles from 30 to 90 mrad.

Particle identification will improve the accuracy of the reconstruction of events on the ILC, and together with the precise measurement of luminosity will allow to measure the cross sections of the reactions of liquid events.

1.3 LumiCal detector

LumiCal detector — cylindrical electromagnetic calorimeter is designed to measure luminosity in ILC and CLIC (Compact Linear Collider) projects with an accuracy of $\frac{\Delta L}{L} = 10^{-3}$. Its location in the ILD detector shown in Fig. 1.2 It is located in the gap of the ECAL detector and covers the polar angles from 30 to 90 mrad.It is a sandwich-type calorimeter and consists of 20 (30) layers of sensor-absorber for ILD (CLIC) project.

The absorber consists mainly of tungsten (95 %) with impurities of nickel (2.5 %) and copper (2.5 %). Its thickness is 3.5 mm, which is approximately equal to one radiation length of $1X_0$.

The sensor is a Si semiconductor. It has the shape of a sector of a circle with an inner radius of 80 mm and an outer 195.2 mm. One sensor occupies a 30° azimuthal angle and is divided into 4 azimuthal sectors of 7.5°. 12 sensors completely cover the azimuthal angle. Radially, each sector is divided into 64 pads. The structure of one sensor is shown in Fig. 1.3.

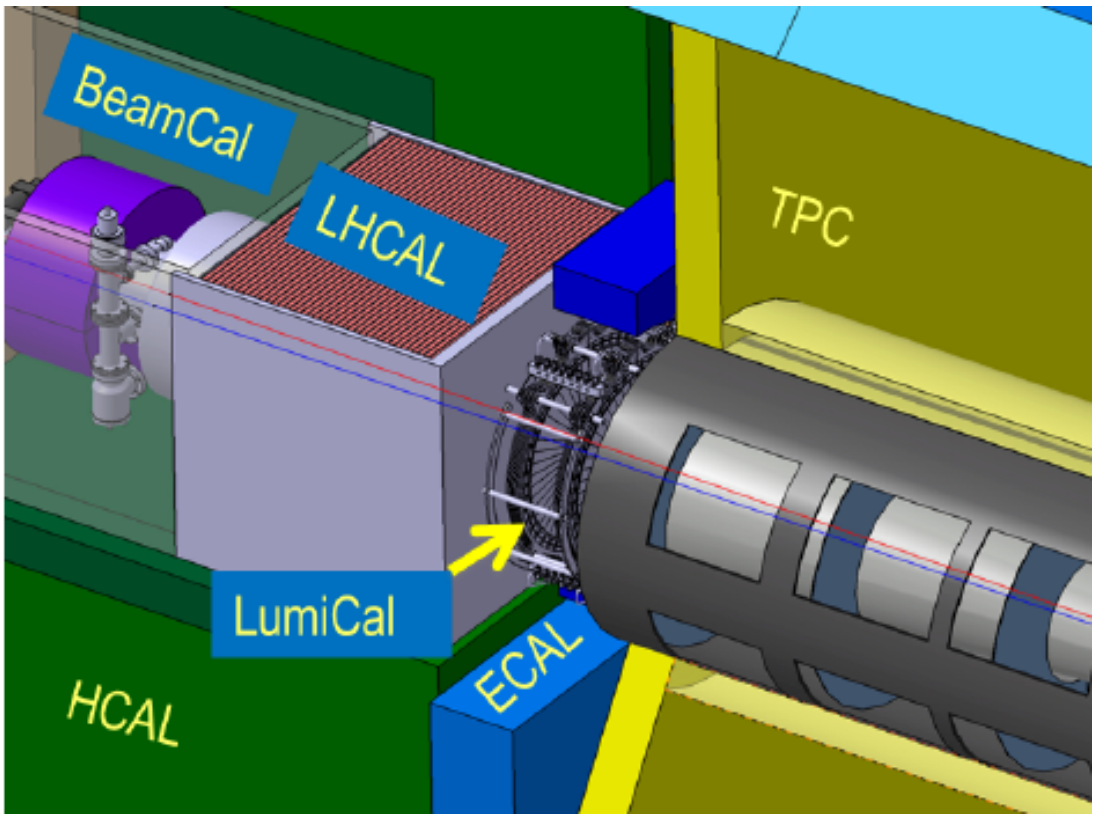

Figure 1.2: Location of LumiCal in the ILD detector.

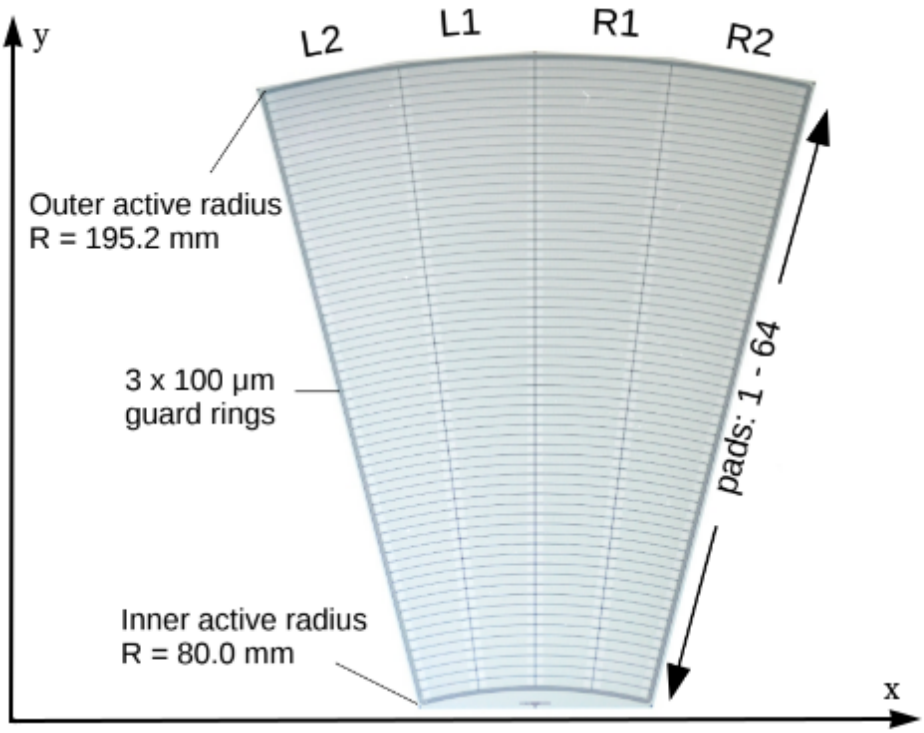

Figure 1.3: Structure of one Si LumiCal detector sensor.

The LumiCal detector is designed to accurately measure luminosity by counting Bhabha

scattering events $e^+e^- \to e^+e^-(\gamma)$. The cross section of this reaction is known t

$$\frac{d\sigma_B}{d\theta} = \frac{2\pi\alpha_{em}^2}{s}\frac{sin(\theta)}{sin^4(\frac{\theta}{2})} \approx \frac{32\pi\alpha_{em}^2}{s}\frac{1}{\theta^3}, \tag{1.1}$$

where $\alpha_{em} = \frac{1}{137}$ is the fine structure constant , s is the energy of the center of mass system, θ is the scattering angle of the electron.

Then, the luminosity is calculated by the formula: $L = \frac{N_B}{\sigma_B}$, where N_B — the number of registered events with Bhabha scattering, σ_B" — theoretically calculated cross section of Bhabha scattering reaction with restriction of polar angles by the LumiCal detector.

LumiCal can potentially distinguish charged particles from neutral ones. To do this, the first few calorimeter sensors must be left without absorbers so that they play the role of a tracker. This would extend the tightness of the ILD detector to small polar angles and improve the reconstruction of events.

Particle identification would be as follows: if the tracker has signals corresponding to a shower in the calorimeter — charged particle; if the tracker does not have signals that would correspond to a shower in the calorimeter" — neutral.

One of the problems that can interfere with the correct identification of a particle is the spurious signals in the tracker sensors from the secondary particles scattered back from the calorimeter. Therefore, it is of practical interest to study the nature and number of backscattered particles that would be detected by the tracker sensors, as well as to investigate their effect on particle identification. This was done by the author in this paper and allowed to test the possibility of extending the tightness of the ILD detector to small polar angles.

2 LumiCal Data Analysis

Data from the LumiCal calorimeter test on the DESY-II accelerator in 2016 [7; 8] were used to study the nature of backscattering and its effect on particle identification.

The data were compared with Monte Carlo simulations made in Geant4 version 4.10.5 [9–11].

All the results presented in this paper were obtained using ROOT libraries, which are widely used in high-energy physics [12].

2.1 Experiment geometry on DESY-II accelerator

In Fig. 2.1 shows the geometry of an experiment to test a LumiCal calorimeter on a DESY-II accelerator. At the output of the DESY-II accelerator, electrons with energies of 1-6 GeV are fed, which pass through a collimator measuring 5×5 mm.

The following equipment was located in the direction of electron flight:

- 3 scintillators Sc1, Sc2, Sc3. They worked as a trigger in the matching scheme.
- Tg. 1.5 mm thick copper target to generate a beam of brake gamma quants. It was present only in the recording of data with two beams — electrons and bremsstrahlung gamma quants. In events with one beam of electrons, the target was absent.
- Magnet. When recording data with an electron beam, it was turned off. It was turned on when recording data with a Tg target to deflect electrons from the flight path of braking gamma quants and to form two separate showers in the calorimeter.
- T1, T2 two arms of the DATURA telescope with pixel detectors MIMOSA-26 [7]. The telescope was used to align the relative position of the equipment. The resolution of the telescope and its distance to the LumiCal detector did not allow its use as a tracker to reconstruct the position of the particle in the calorimeter.
- Prototype of a LumiCal detector, which investigated the propagation of the rain in the calorimeter and the identification of particles using a tracker.

The LumiCal prototype consisted of 8 sensors and 9 absorbers, as shown in Fig. 2.1. The first two sensors were moved forward from the calorimeter to act as a tracker and identify particles. Therefore, the first sensor in the calorimeter is located after the three

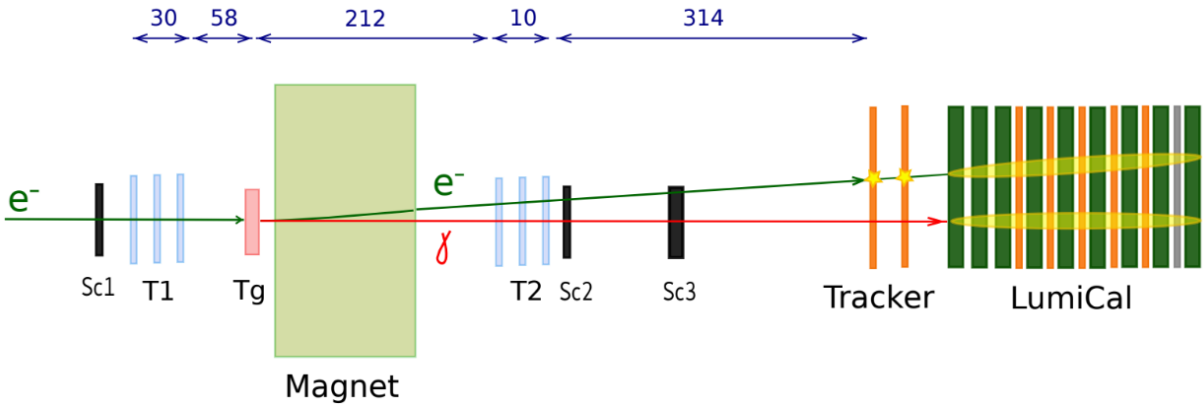

Figure 2.1: Geometry of equipment location and LumiCal calorimeter tested on DESY-II accelerator. Distances in centimeters are shown at the top.

absorbers. The last sensor is located after eight absorbers, which corresponds to a radiation length of $7.7X_0$, because the absorbers contain impurities of other elements.

The sensors and absorbers were located in a special box and were fixed in the grooves equidistant from each other by 4.5 mm. The layer of air between two adjacent layers of the calorimeter was 1 mm. Fixing of absorbers and sensors in grooves of a special box is visible in Fig. 2.2.

All sensors were located in a special carbon frame, which was glued to the front of the absorbers. The last sensor was glued by the method of TAB (Tape automatic boding), due to which there was an increased noise level. Therefore, it was not used in this analysis.

A return voltage of 120 V was applied to the sensors. This is 2-3 times higher than the saturation voltage and much lower than the breakdown voltage.

The sensors were connected to APV-25 readers with 128 channels [13]. Thus, two APV-25 interfaces were connected to each sensor.

This analysis uses two types of measurements performed during testing

- **Electrons only**: Beam of 5 GeV electrons, no target for generating bremsstrahlung gamma quants, magnet off
- **Electrons with bremsstrahlung gamma quants**: Beam of 5 GeV electrons, a target for the generation of bremsstrahlung gamma quants, a magnet with a magnetic field of about 0.9 T. The magnet deflected the electron beam and they were recorded in the calorimeter by an average of 2 cm lower than the beam of bremsstrahlung gamma quants.

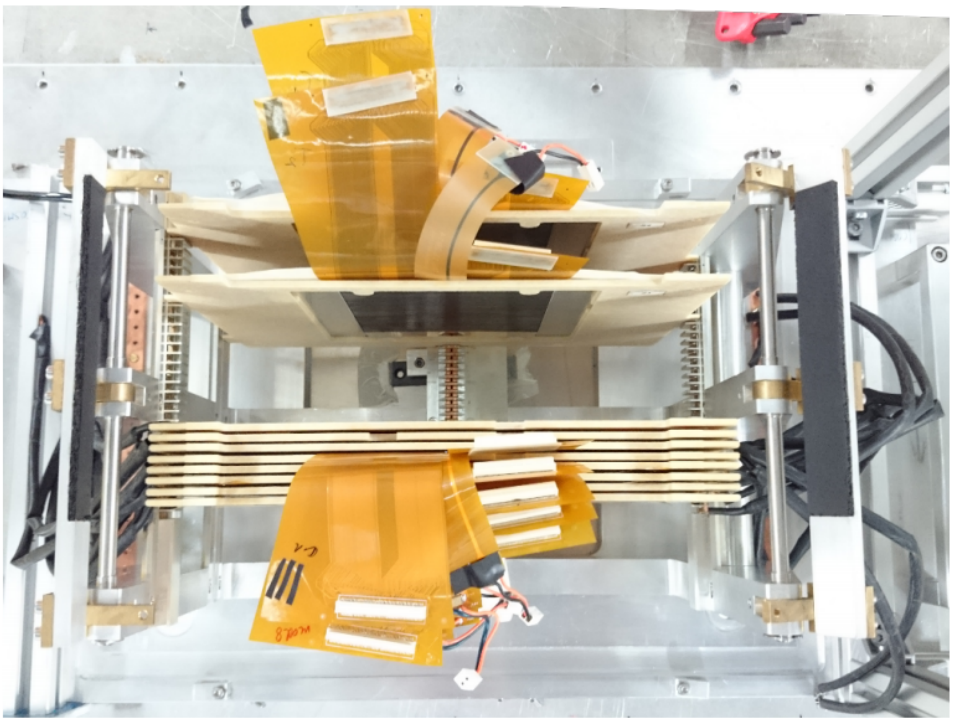

Figure 2.2: Top view of LumiCal detector sensors and absorbers located in the slots of the box. Detached sensors at the top act as a tracker.

2.2 Reconstruction and selection of signals

When the particle passes through the Si sensor, a current peak is generated. The APV-25 reader electronics have a CR-RC integrated circuit that converts the current peak into a voltage peak with a shape that reflects the response function. APV-25 measures signals from the sensor asynchronously in 21 consecutive time intervals. An example of the signal is shown in Fig. 2.3.

The reference signal APV-25 is calculated as the average of all 21st time intervals with the beam off. The noise value for each APV-25 channel is calculated as the standard deviation of the signals in the 21st time intervals with the beam off.

The noise value is used not to record all channels in a row, but only those where there was a signal that exceeds a certain threshold. A signal is recorded if the average value of 21 signals in consecutive time intervals is more than 40 % of the noise value for this channel.

This threshold is quite small and allowed a lot of noise. Therefore, to determine the presence of the signal and its maximum signals from 21 consecutive time intervals are

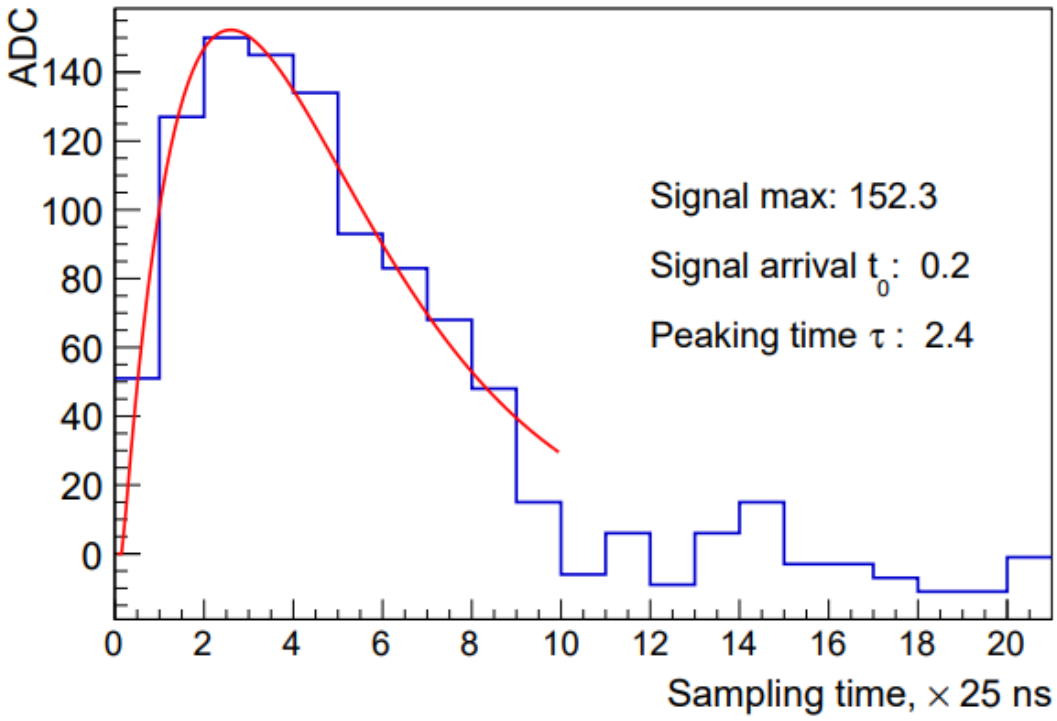

Figure 2.3: The signal from the particle is divided into 21 time intervals of 25 ns. Red line — approximation of the waveform.

approximated by the response function:

$$S(t) = A\frac{t - t_0}{\tau}e^{-\frac{t-t_0}{\tau}}\Theta(t - t_0), \tag{2.1}$$

where t_0 is the time of arrival of the signal, τ is the time at which the signal becomes maximum, A signal amplitude, $\Theta(t - t_0)$ — Heaviside function.

To classify the signal, a neural network was used, which is a perceptron with 21 input parameters from APV-25 time slots and has one hidden layer with 10 nodes. At the output of the neural network, the probability is obtained that the signal is left by the particle.

Only signals that underwent the following selection were admitted to the analysis:

- $1 < \tau_{fit} < 3$ — the time to reach the maximum must be in the expected region for the signal from the particle.
- $S_{max} < 2000$ ADC — APV-25 registration limit, signals above 2000 ADC (Analog-Digital Counts) cannot be.
- $t_{1,bin} - 2.7 < t_{0,fit} < t_{1,bin} - 0.5$ — The signal arrival time corresponds to the expected arrival time set from $t_{1,bin}$ - bean time with maximum signal.

- $NN_{output} > 0.5$ — a trained neural network gives more than 50 % probability that the signal is from a particle.

Each sensor had all 256 pads connected to the reading electronics. Two left sectors were read by 128 channels of one APV-25, two sectors on the right — another. But not all pads were the region of interest for this analysis, so signals from certain pads were not taken into account. Fig. 2.4 shows the pads in each sensor that did not participate in the analysis in red. The following are the reasons for excluding these pads from the analysis:

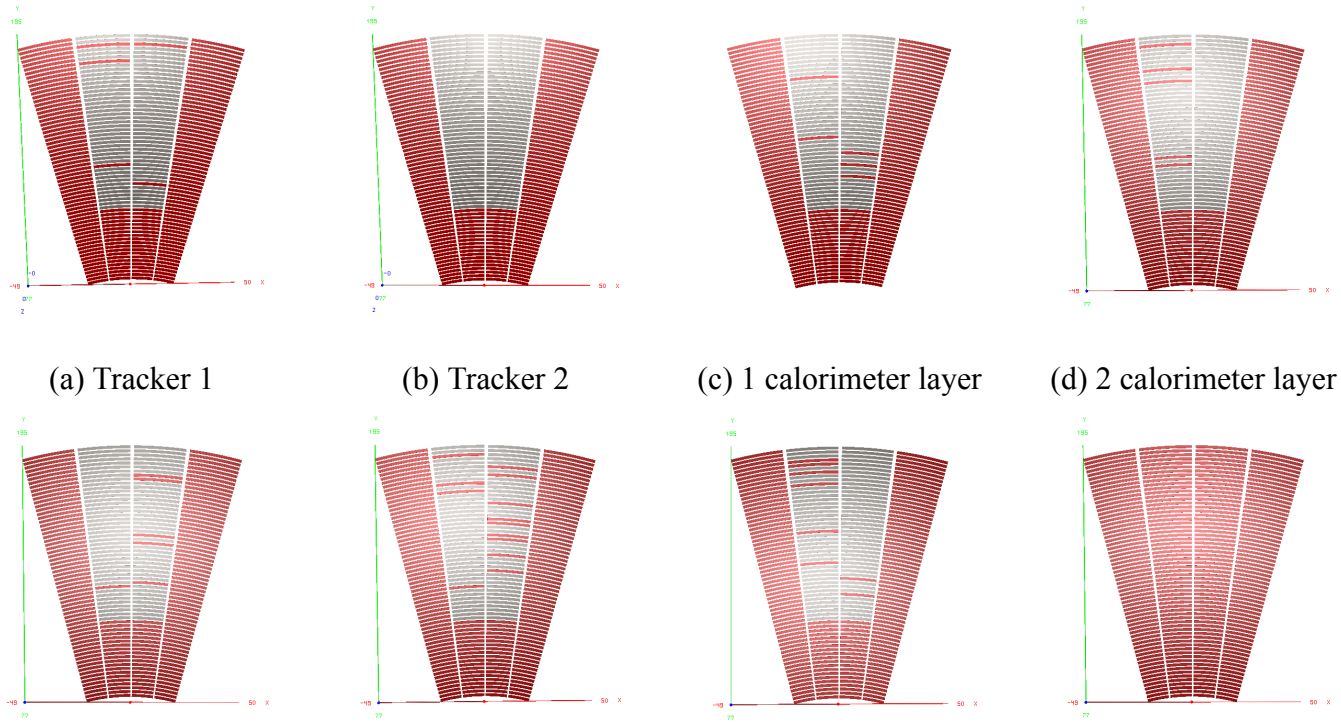

(a) Tracker 1 (b) Tracker 2 (c) 1 calorimeter layer (d) 2 calorimeter layer

(e) 3 calorimeter layer (f) 4 calorimeter layer (g) 5 calorimeter layer (h) 6 calorimeter layer

Figure 2.4: White — pads used in analysis. Red — pads not used for analysis

1. **Side sectors:** The width of the electron beam at the entrance to the calorimeter is less than 10 mm, given the effective Moliere radius of the calorimeter, which is 8 mm [8], we do not expect signals further than 18 mm from the center of the beam. The horizontal length of one sector of size 7.5° at the height of the 45th drop is 21 mm. This means that the entire shower fits into the two central sectors of our detector. Rare signals recorded in the side sectors are just electrical noise. Therefore, they were excluded from the analysis.
2. **Bottom pads:** Because the APV-25 electronics were designed for a tracker, not a calorimeter, it is not used to measure large signals. Cross-talk between APV-

25 channels was observed during testing. If the APV-25 channel receives a large signal, this signal migrated to neighboring channels, which caused the appearance of a spurious signal 32 drops below the registration of a large signal. During the tests, the presence of a large spurious signal was observed in the region of the lower falls, so the falls below the 20th number were excluded from the analysis to prevent the registration of the spurious signal.

3. **Last calorimeter layer:** As mentioned above, the last sensor in the calorimeter was glued to the absorber by TAB [8] technology. During testing, the sensor had high noise values, so it was not analyzed.

4. **Bad pads:** Single red pads in the middle of the white region of the sensor shown in Fig. 2.4 — pads with constant and high noise levels relative to the particle signal. Therefore, in order not to record noise continuously, they were also excluded from the analysis.

2.3 Calorimeter shower reconstruction algorithm

This section describes in detail the algorithm for reconstructing the position of the drains in the calorimeter. The cluster algorithm was also applied to the signals in the tracker to correctly account for particles that passed between the two pads, leaving two hits.

Each cluster in the calorimeter describes the propagation of the downpour from the particle entering the calorimeter. The clustering procedure is necessary because the clusters carry information about the energy of the particle and its input position in the calorimeter, when individual hits do not carry such information.

The cluster algorithm creates clusters based on towers.

The tower is a group of all falls in the longitudinal direction with the same position in the perpendicular plane. The energy of the tower is the sum of the energies in all the falls inside the tower.

For example, visually the tower is illuminated in green in Fig. 2.5.

The following is a step-by-step description of the cluster algorithm:

1. Make all towers with a local maximum energy and more than one active drop inside the tower with a grain cluster.

2. Sort towers in descending order.

3. For each tower that is not yet assigned to any cluster:

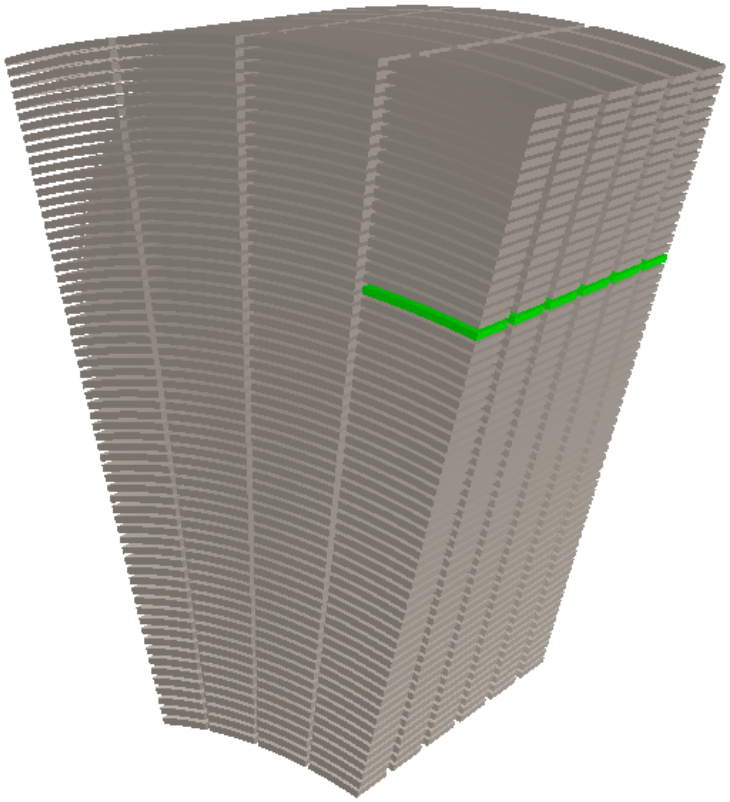

Figure 2.5: The particular tower is highlighted in green.

   (a) Find all adjacent towers ($\pm$ 1 pad and $\pm$ 1 sector) that are already attached to a specific cluster.
   (b) If found: Assign the current tower to the cluster of the neighboring tower.
   (c) If not found: skip and continue for the next tower without a cluster.

4. Increase the radius of the neighborhood by one and repeat (3).
5. Repeat (4) until all towers join some clusters.
6. Merge pairs of clusters if the merge condition is met (see below).

The explanation of the algorithm by example is given in Fig. 2.6. It shows the intermediate steps of the algorithm on the example of one event with a single 5 GeV electron, which leaves a signal in the calorimeter.

- **a:** Towers with registered energies in the calorimeter. You can see 4 towers with a local maximum energy in this event, but only 2 of them have more than one active pad inside the tower.

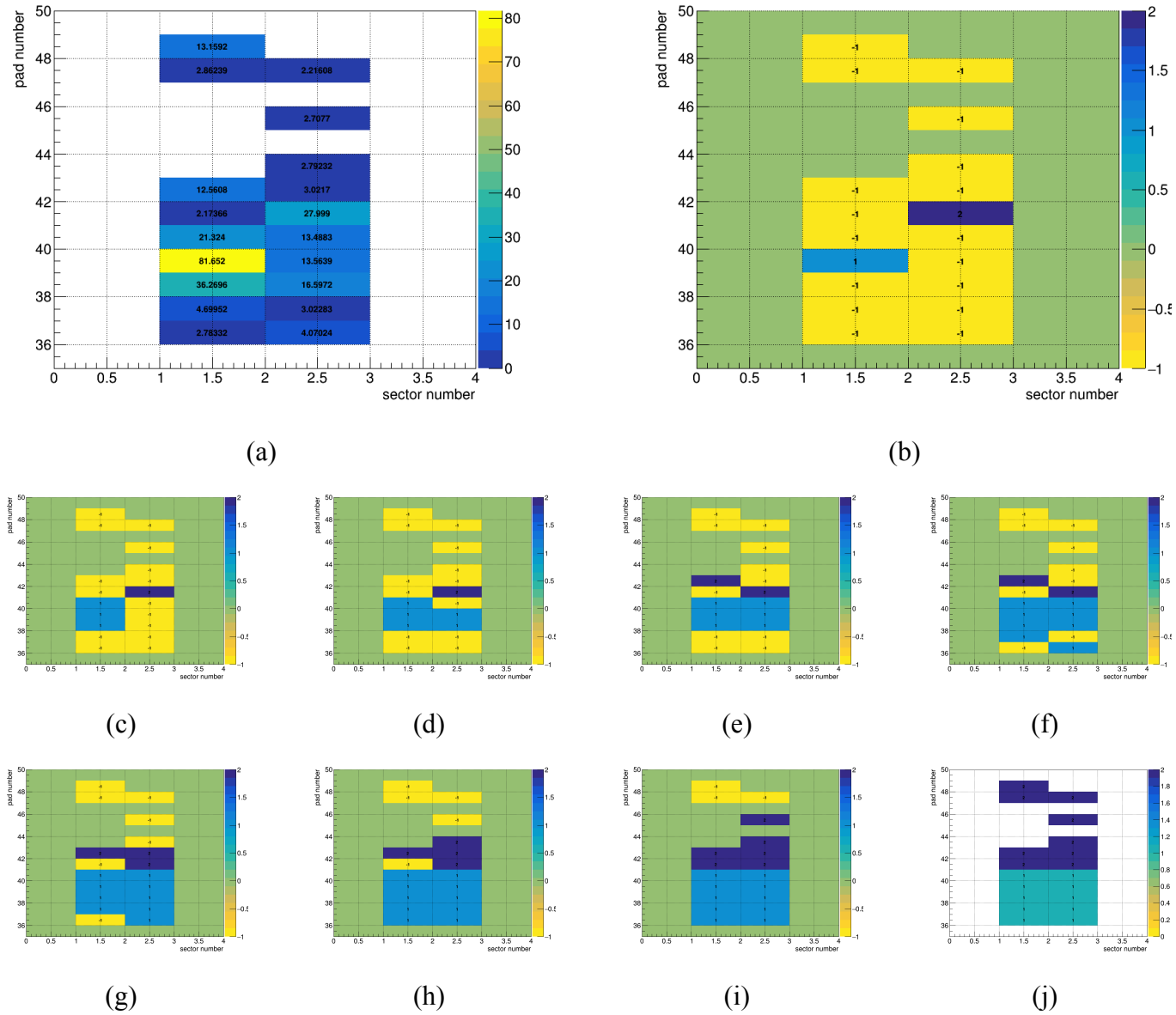

Figure 2.6: (a) shows the recorded energy in the calorimeter towers. (b-i) shows how the towers combine and form clusters during the steps of the algorithm. ”- 1” — the tower is not assigned to any cluster.” 1,2, ... ”” — cluster index to to which the tower belongs.

- **b:** 2 cluster grains are formed.
- **w:** Loop through all towers without cluster (-1) and gradually join the towers with the cluster.
- **c:** All neighboring towers have a cluster. To connect separate towers, the neighborhood distance is increased by one.
- **and:** Two final clusters. Since in this event only one particle flies into the calorimeter, the expected number of clusters (drains) is one. To adjust the algorithm, in cases

where it sees more particles than it actually has, a fusion of clusters is performed that is very close to each other or with a high energy ratio. In this case, the clusters will be merged, because the distance between them is 7.73 mm, and the energy ratio is 0.35, which satisfies the conditions described below.

The cluster algorithm described above in paragraphs (1) to (5) was analyzed with LumiCal test data with one 5 GeV electron, where only 1 reconstructed drain (cluster) in the calorimeter was expected.

Figure 2.7a shows the number of reconstructed clusters in events without cluster merging, only using algorithm (1) - (5). As a result, 39 % of events were reconstructed with more than one cluster, which is not the expected result.

To prevent this, we merge pairs of clusters depending on the distance between them and their energy ratio.

The conditions for the merger are as follows:

- **Distance:** if the distance between the clusters is less than the Moliere radius (8 mm) then it is probably the same shower, which is separated due to the shortcomings of the electronics, and so on.
- **Energy ratio:** If the energy ratio of a smaller energy cluster to a smaller energy cluster is small, then probably a smaller energy cluster is only a separation from a large shower, not a separate shower from a particle.

Fig. 2.7b shows the ratio of energies and the distance between the two most energy clusters in single electron events. The red line shows the boundary within which the largest number of artificial clusters is located. This border is our condition for merging.

Fig. 2.7b shows that most artificial clusters are located closer than 7.5 mm to the most energy cluster. And the energy of artificial clusters is about 5 % of the energy of the main cluster.

Thus, we supplement our clustering algorithm by merging clusters with the following conditions:

- $|y_1 - y_2| < 7.5$ mm, or
- $\frac{E_2}{E_1} < 0.032 \cdot (20 - |y_1 - y_2|)$

A merger reduces the number of events with more than one reconstructed cluster (artificial clusters) from 39 % without a merger to 2.8 % with a merger.

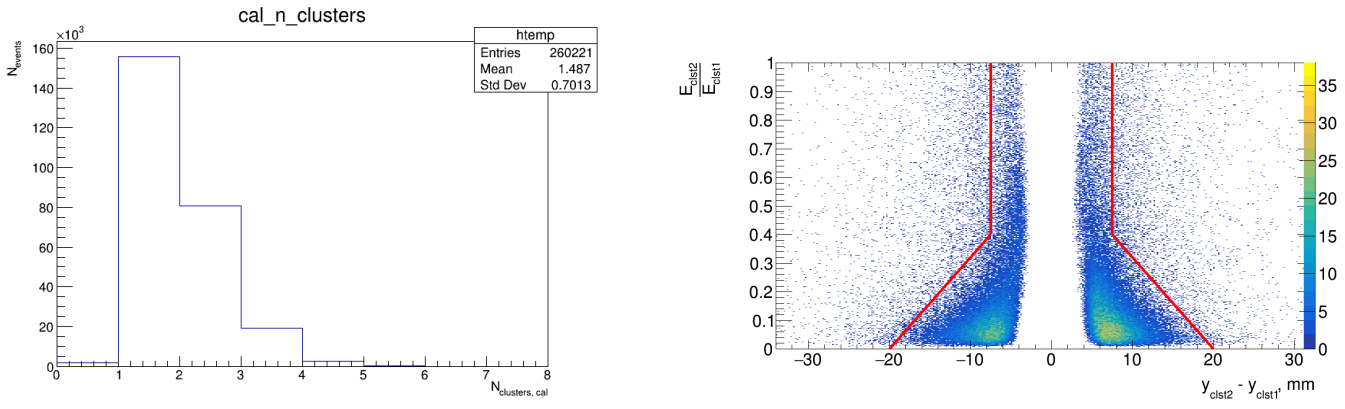

(a) (b)

Figure 2.7: (a) Number of reconstructed clusters in the calorimeter without merging. (b) The distance and ratio of energies between the two most energy clusters in events as a 2D histogram. Pairs inside red lines will be merged into one cluster by the algorithm.

Hits in the tracker were also clustered by a simpler and similar algorithm.

This is necessary because sometimes, a particle passes between two pads leaving signals in both. To prevent this event from perceiving two neighboring signals from one particle as two particles, all neighboring hits were reconstructed as one cluster.

Step-by-step algorithm for cluster algorithm in tracker:

1. All hits with a local maximum energy make the grain cluster.
2. Sort hits by decreasing energy.
3. For each hit that has not yet been assigned to any cluster:
   (a) Find all neighboring hits ($\pm$ 1 pad and $\pm$ 1 sector) that are already attached to a specific cluster.
   (b) If found: select the most energetic neighbor and assign the current hit to the cluster of the next hit.
   (c) If not found: skip and continue for the next hit without a cluster.

This algorithm is the same as for the calorimeter, but with some differences:

- No cluster merge because there is no drain in the tracker.
- We do not need more than one active pad in the tower to create a cluster grain, as there are no towers.

- Steps (4) - (5) have been deleted, because after step (3) all hits will already be assigned to clusters.

The position of the cluster in the calorimeter is determined by the method of logarithmic weighing. This method shows better resolution than linear energy weighing [8].

$$y_{cluster} = \frac{\sum_i y_i \cdot w_i}{\sum_i w_i}, \tag{2.2}$$

where and runs all the pads included in the cluster. y_i - the position of the pad and w_i weight, which are calculated by the following formula:

$$w_i = max(0, W_0 + ln\frac{E_i}{\sum_i E_i})), \tag{2.3}$$

where W_0 is a dimensionless parameter that specifies the energy level at which the falls will not be included in the calculation of the position of the shower. The value $W_0 = 3.4$ gives the best vertical position resolution for the LumiCal calorimeter, which was investigated in the Geant4 simulation.

Clusters in the tracker mainly consist of only one or two pads and there is no point in using logarithmic scales. Energy weighing was used to reconstruct the position in the tracker.

$$y_{cluster} = \frac{\sum_i y_i \cdot w_i}{\sum_i w_i} = \frac{\sum_i y_i \cdot E_i}{\sum_i E_i} \tag{2.4}$$

2.4 Comparison of data with Geant4 simulation

This section presents comparative distributions by number of detected particles, position and energy for LumiCal calorimeter test data and their modeling in Geant4.

In Fig. 2.8 shows the number of reconstructed clusters in the first tracker and calorimeter in events with one 5 GeV electron. In more than 90

The particle number distributions in the first tracker and calorimeter for data and simulations of events with electrons and bremsstrahlung gamma quants are shown in Figs. 2.9. There is only one cluster of electrons in the tracker, because gamma quants, like neutral particles, do not leave a signal there. And in the calorimeter about 30 % of events have two clusters. The second clusters are created by bremsstrahlung gamma quants, which were able to pass three absorbers and leave enough energy to form a downpour for the algorithm to reconstruct their hits as a cluster.

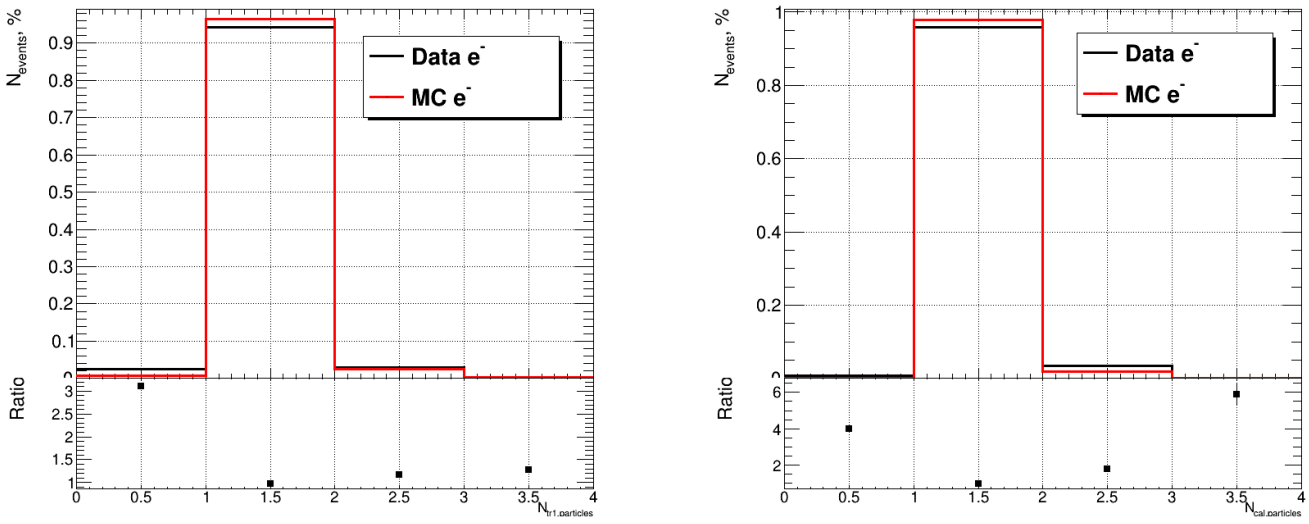

(a) (b)

Figure 2.8: Number of particles recorded by tracker 1 (a) and calorimeter (b) in events with one 5 GeV electron.

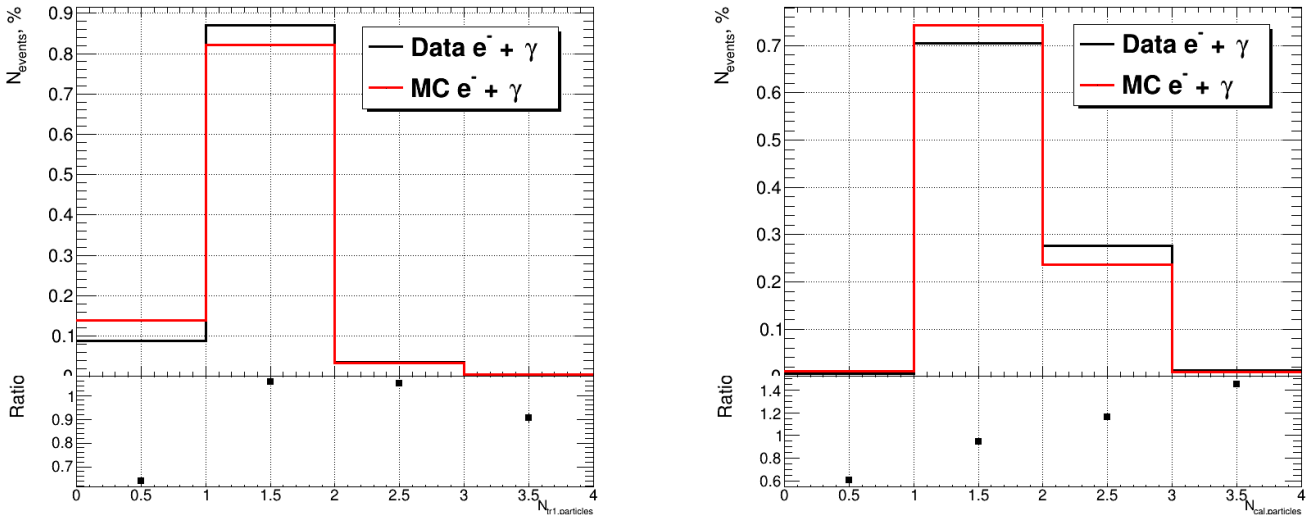

(a) (b)

Figure 2.9: Number of reconstructed particles in the first tracker (a) and calorimeter (b) in electron and brake gamma-ray events.

Fig. 2.10 shows the reconstructed vertical position of the drains in the calorimeter. The peak of about $y = 140$ mm corresponds to the plum of the electron that was deflected by the magnet from the initial direction. The peak with $y = 170$ mm corresponds to the downpour of brake gamma quants. The distance between the showers is 1-3 cm, which allows you to study the identification of particles with a simple scenario without crossing

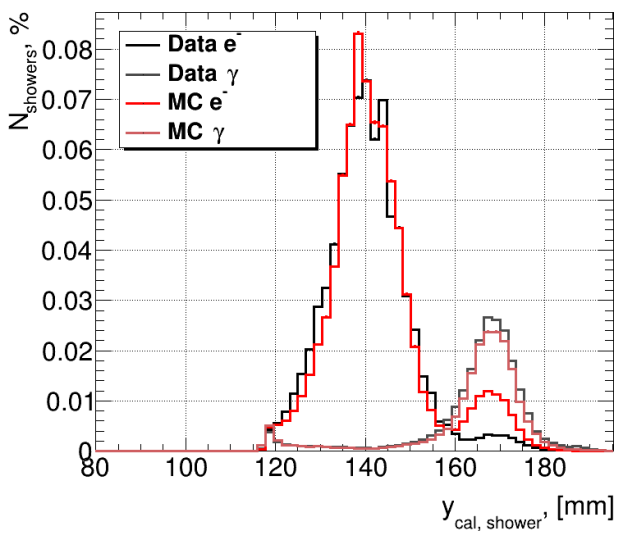

(a)

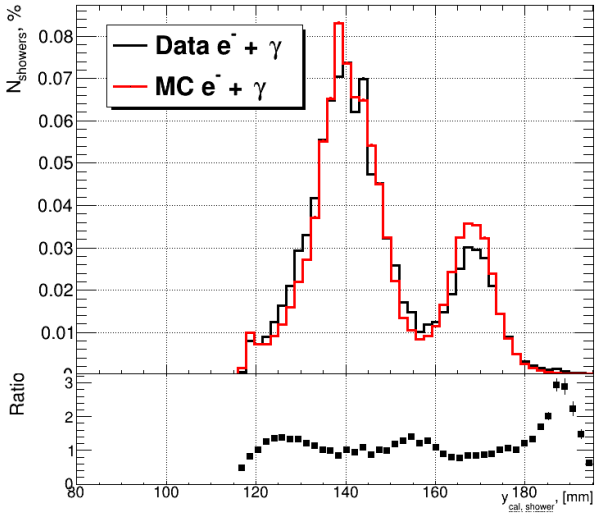

(b)

Figure 2.10: (a) The position of the reconstructed two most energy clusters in the calorimeter. (b) Their sum with the ratio of data to the Geant4 model.

several showers.

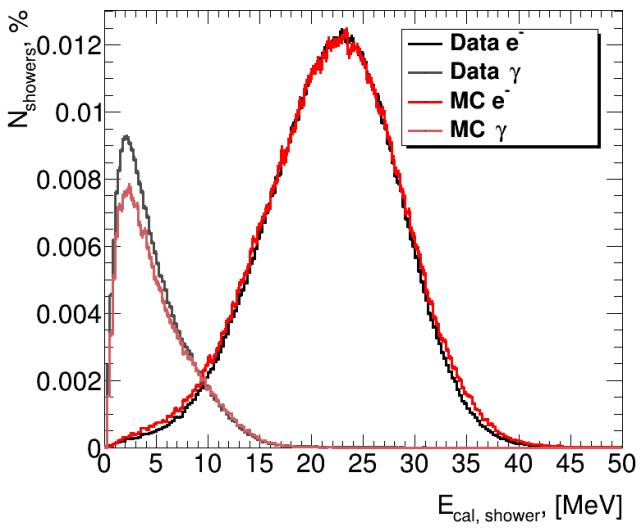

(a)

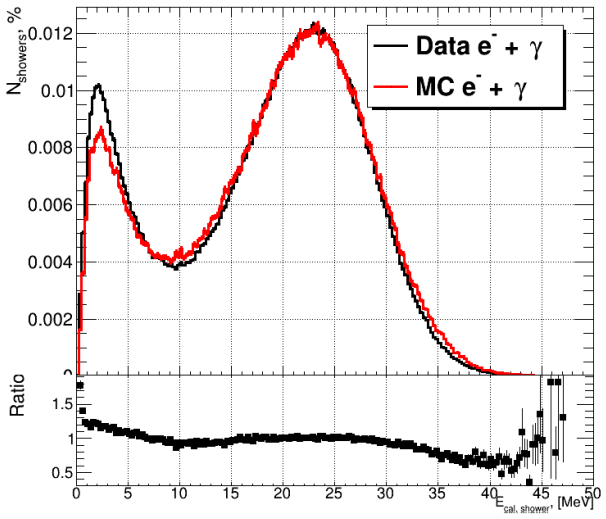

(b)

Figure 2.11: (a) Energy is stored in the LumiCal calorimeter sensors from two electron showers and braking gamma rays. (b) Their sum with the ratio of data to the Geant4 model.

In Fig. 2.11 shows the energy distribution of electron and braking gamma rays. Electrons with an energy of 5 GeV leave in the Si calorimeter sensors approximately 23 MeV of energy with a large width of distribution due to the corresponding energy resolution of

the detector. bremsstrahlung gamma quants leave the corresponding hyperbolic spectrum. The energy limit below and the corresponding peak are caused by the presence of three absorbers in front of the first calorimeter sensor, which makes it impossible to register the downpour of low-energy gamma quants.

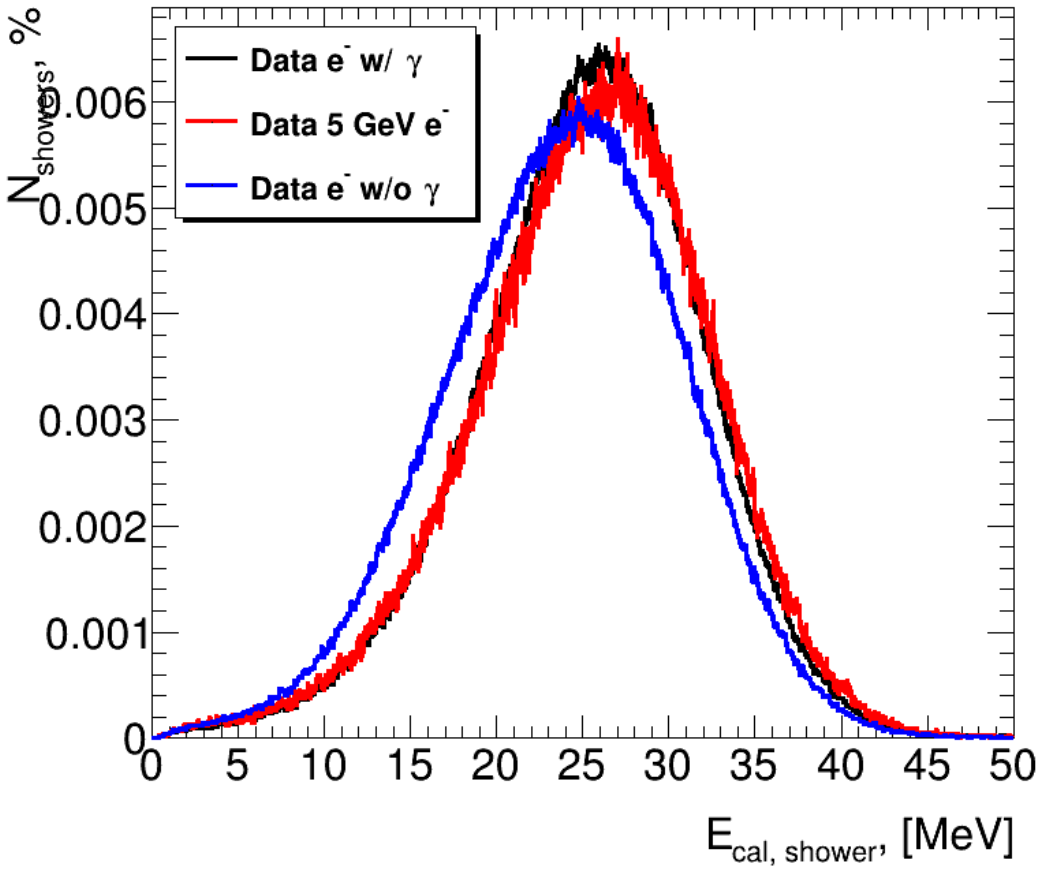

Figure 2.12: Energy left in calorimeter sensors in events with one 5 GeV electron compared to events with photon and braking photons.

A good check of the correct measurement is shown in Fig. 2.12. It presents the sum of the energies of the electron and brake gamma quants drains in comparison with the electron drain energies in events without brake gamma quants. We see that the energy of a 5 GeV electron is preserved, even if part of it is transferred to another discharge of bremsstrahlung gamma quants.

In summary, it should be noted that the comparative distributions of simulations in Geant4 and data agree with each other. Some discrepancies are seen due to the shortcomings of the simulation of experimental details in Geant4, but these discrepancies are not significant for particle identification and backscattering analysis.

Because the Geant4 simulation correctly describes the distributions observed in the

experiment, further study of backscattering and particle identification will use information from the Geant4 simulations.

2.5 Back scattering

The backscattered particles from the calorimeter can generate spurious signals in the tracker sensors. This can lead to incorrect particle identification, which is of practical interest for studying the nature of backscattering.

This section presents the results of the analysis of the nature and number of backscattered particles observed in the tracker sensors.

The following distributions were obtained and investigated using simulation in Geant4:

1. Tracker registration frequency
2. Particle type
3. Particle energy
4. Energy is registered by the tracker
5. Angular particle distribution
6. Distribution of hits in the tracker relative to the downpour

Table 1 shows how often particles of each type are found in the tracker sensors.

The tracker records 2.5 times more directly scattered particles from the experimental equipment than backscattered particles from the calorimeter. We will be interested in them, because this is a characteristic of the geometry of the experiment, and backscattering — a characteristic of the detector.

The first tracker registers 5 % less primary electrons than the second, because the first has several bad pads that were excluded from the analysis due to high noise. Due to this, a certain number of signals are lost.

Backscattered particles, mainly electrons (1.53 %) with a fraction of gamma rays (0.79 %), positrons (0.26 %) and hadrons (0.02 %). The second tracker registers more events with backscattered particles than the first tracker, which again indicates that the source of these particles is on the side of the calorimeter.

In total, 2.55 % of events with backscattered particles were registered in the second sensor of the tracker, which is closer to the calorimeter.

Number of events, %		
Particle Type	Tracker 1	Tracker 2
Primary e^-	$84.937 \pm 0.008\%$	$89.994 \pm 0.007\%$
Straight-scattered e^-	$2.796 \pm 0.004\%$	$4.63 \pm 0.005\%$
Straight-scattered e^+	$2.028 \pm 0.003\%$	$2.445 \pm 0.003\%$
backscattered e^-	$0.993 \pm 0.002\%$	$1.528 \pm 0.003\%$
backscattered γ	$0.499 \pm 0.002\%$	$0.792 \pm 0.002\%$
Straight-scattered γ	$0.606 \pm 0.002\%$	$0.684 \pm 0.002\%$
backscattered e^+	$0.14 \pm 0.001\%$	$0.256 \pm 0.001\%$
backscattered hadrons	$0.0146 \pm 0.0003\%$	$0.0247 \pm 0.0004\%$
Total straight-scattered	$4.198 \pm 0.005\%$	$6.238 \pm 0.005\%$
Total backscattered	$1.619 \pm 0.003\%$	$2.546 \pm 0.004\%$

Table 1: Share of events in which a certain particle type is registered in the corresponding tracker sensor.

In Fig. 2.13 shows the distribution of the vertical projection of the momentum of backscattered particles. Up to a constant, this corresponds to the distribution of backscattered particles at an angle. you can see that all particles have a similar scattering character.

In Fig. 2.14 shows the coordinate distributions of hits from backscattered particles registered by the second tracker. The position of the hits of the backscattered particles is almost uniformly distributed along the plane of the sensor with a slight inclination toward the larger radius. This is due to the increase in the area of the sensor drop with increasing y, which leads to the registration of more particles.

In Fig. 2.15 shows the spectrum of backscattered particles that leave signals in the second tracker. These particles have a flat curve with a gradual decrease in the number of particles with increasing energy. After an energy of 10 MeV the particles are almost imperceptible. The characteristic annihilation peak at 511 keV and the blurred reverse Compton scattering peak at 256 keV are clearly visible.

Fig. 2.16 shows the energies left in the sensor by backscattered particles. The most probable value of this distribution is the residual energy of one MIP (Minimum Ionizing Particle) of the particle, which corresponds to ≈ 88.5 keV for our sensor. The distribution

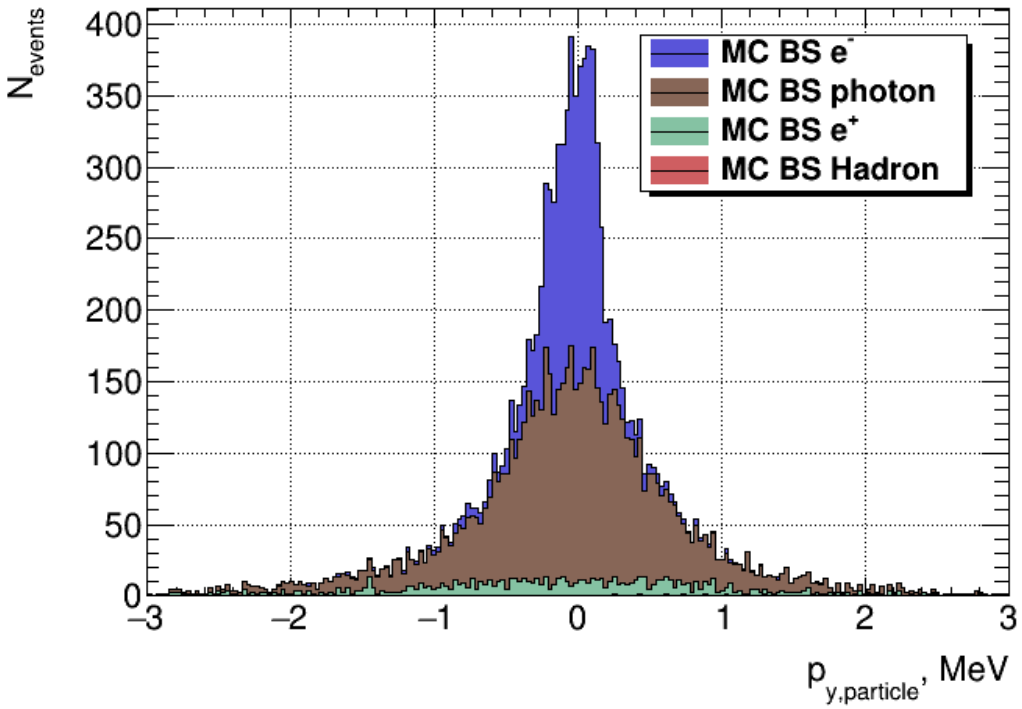

Figure 2.13: Distribution of backscattered particles recorded by the second tracker by pulses along the vertical axis.

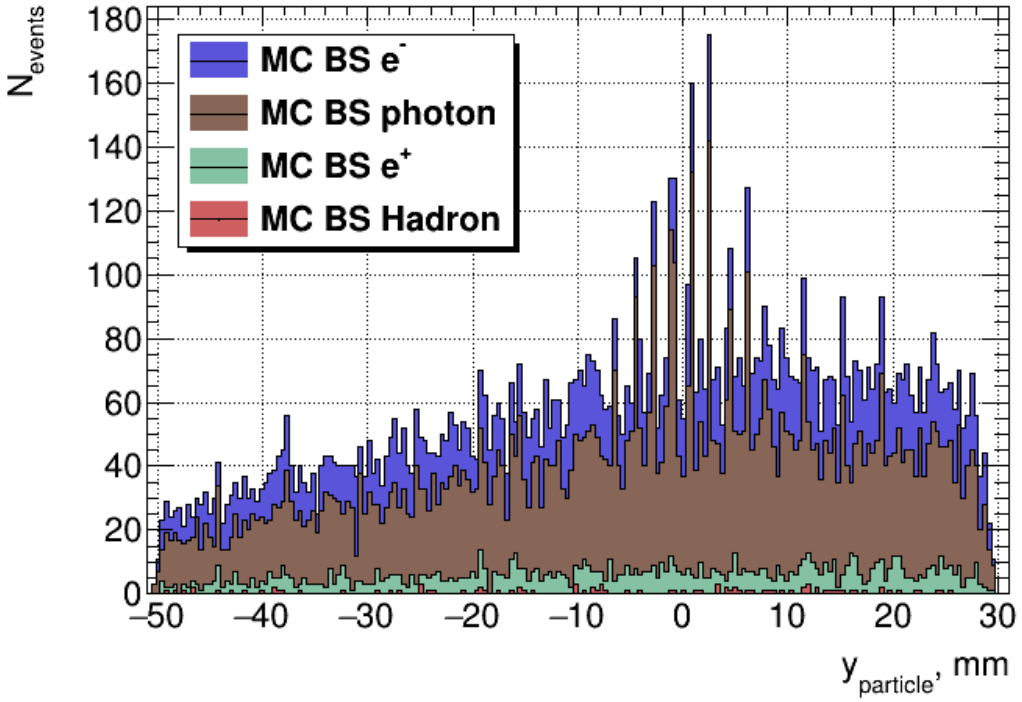

Figure 2.14: Distribution of the vertical coordinate of the hits from the backscattered particles in the second tracker.

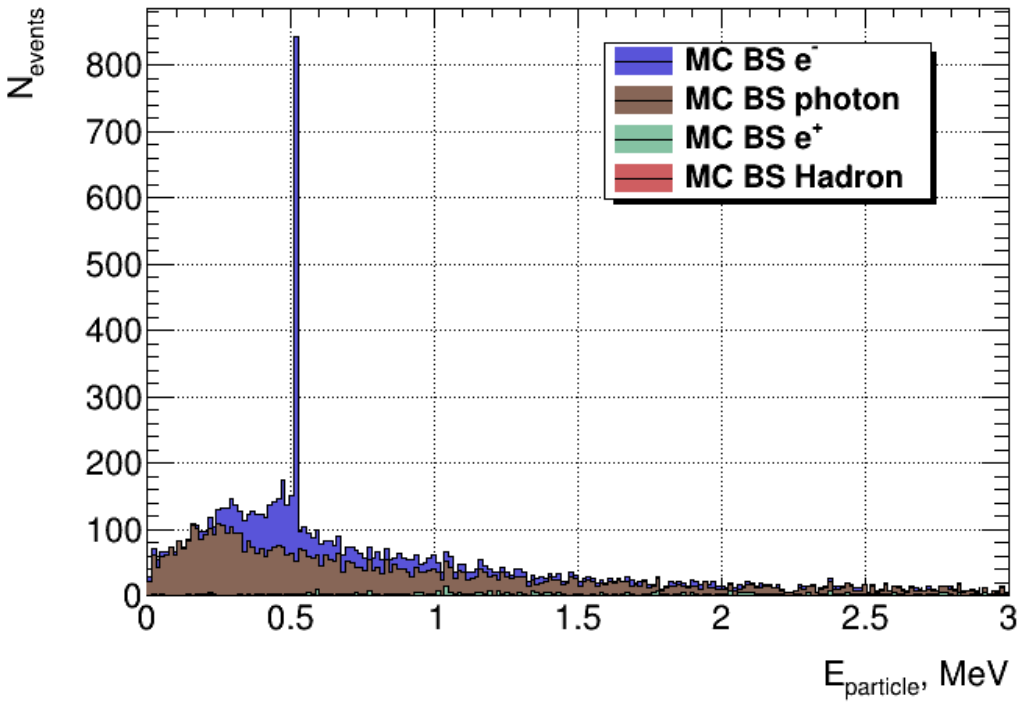

Figure 2.15: Energy of backscattered particles.

looks similar to the energy distribution for the primary 5 GeV electrons.

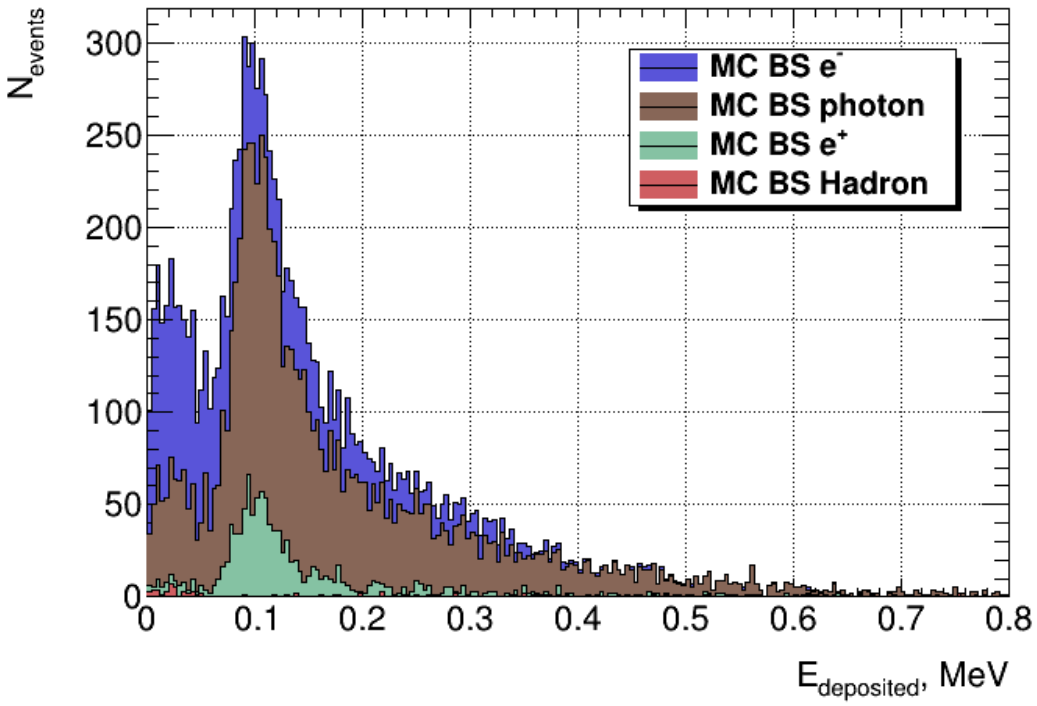

Figure 2.16: The energies recorded by the second tracker are left by backscattered particles.

The distance from the hits in the tracker to the rain in the calorimeter will be used to

identify the particle. Therefore, it is interesting to evaluate how the backscattered particles affect the distribution of the distance from the hit to the shower.

From Fig. 2.17 shows the contribution from the backscattered hits to the distribution of the distance of the hits in the second tracker to the downpour in the calorimeter. The contribution is not noticeable to the eye and is less than one percent.

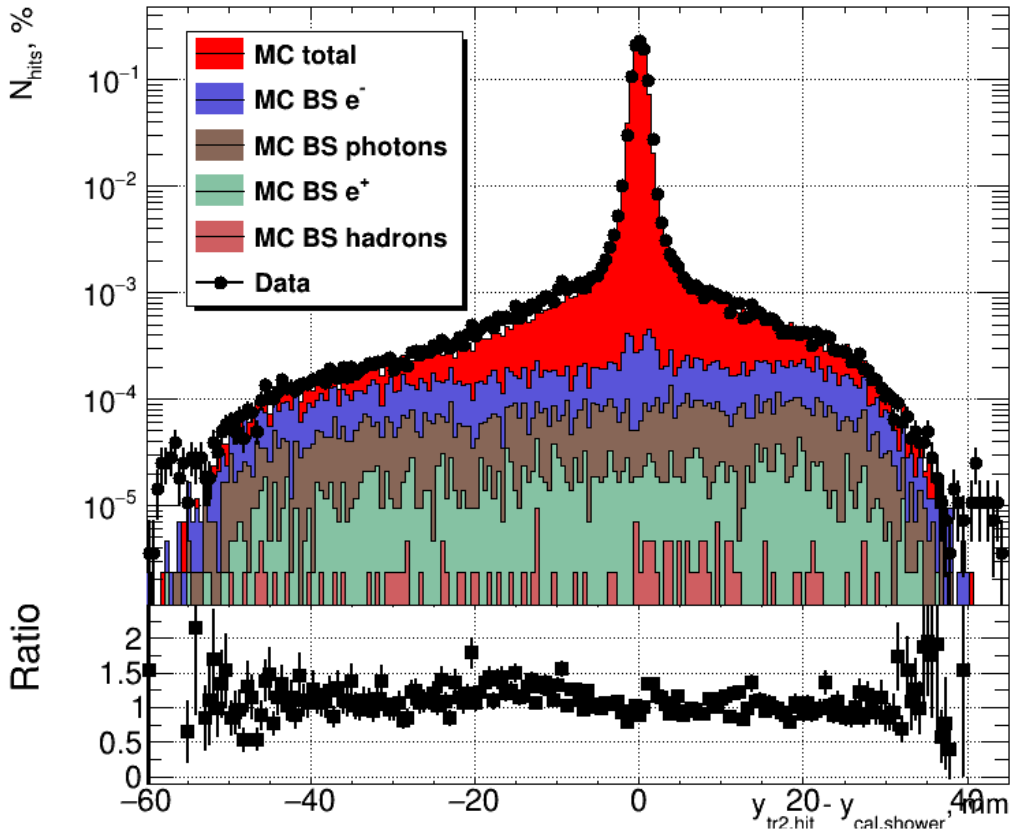

Figure 2.17: Distribution of the distance between hits in the second tracker and the shower in the calorimeter.

2.6 Particle identification

Geant4 simulation was used to study the identification of the type of particle that left the drain in the calorimeter. To study the efficiency of the identification algorithm, events with only two separate reconstructed showers in the calorimeter were selected. It was required that the most energetic shower, which should correspond to the electron deflected by the magnet, be located in the range: $130 < y_1 < 150$ mm. And the second shower, which corresponds to the braking gamma rays, is located within $158 < y_2 < 178$ mm. When it is

known that there were only 2 showers in the event, one from the electron, the other from the gamma quantum, it is possible to investigate the identification algorithm.

The purpose of this work was to investigate the effect of backscattering on particle identification, so all events that had direct scattering were not considered so that the effects of direct scattering and backscattering did not overlap. Thus, according to table. 2 A total of 19,600,000 events were generated, of which 2,515,161 were analyzed for backscattering effects. There were a total of 92,301 backscattering events. This was enough for the statistical error to be small enough to determine the result.

Total generated MK events	19 600 000
Of these, have 2 separate reconstructed showers	2 751 040
+ without direct scattering	2 515 161
+ without backscattering	2 424 860
Total events with backscattering	92 301

Table 2: The number of events that were generated in Geant4 and used in the analysis to study the identification algorithm.

The algorithm identifies the particle by checking the signals in the tracker. If both sensors of the tracker have registered a signal close to the shower in the calorimeter, then the particle is considered an electron, if not, then a gamma quantum. Examples of identification of the shower as electronic and gamma-ray depending on the signals in the tracker are shown in Fig. 2.18.

Depending on the distance at which we attribute the hits in the tracker to the shower in the calorimeter, the efficiency of our algorithm will depend. With a short identification distance, we may not notice some hits. At large, we can capture hits from another shower, or background, backscattered particles, causing efficiency to drop.

To assess the performance of the identification algorithm, define the concepts of efficiency and accuracy:

- $\epsilon = \frac{N_{true^r eco}}{N_{true}}$ — efficiency" — the ratio of the number of electrons (gamma quants) that have been reconstructed and must be reconstructed to the number electrons (gamma quants) that need to be reconstructed.
- $p = \frac{N_{true^r eco}}{N_{reco}}$ — correctness" — the ratio of the number of electrons (gamma quants)

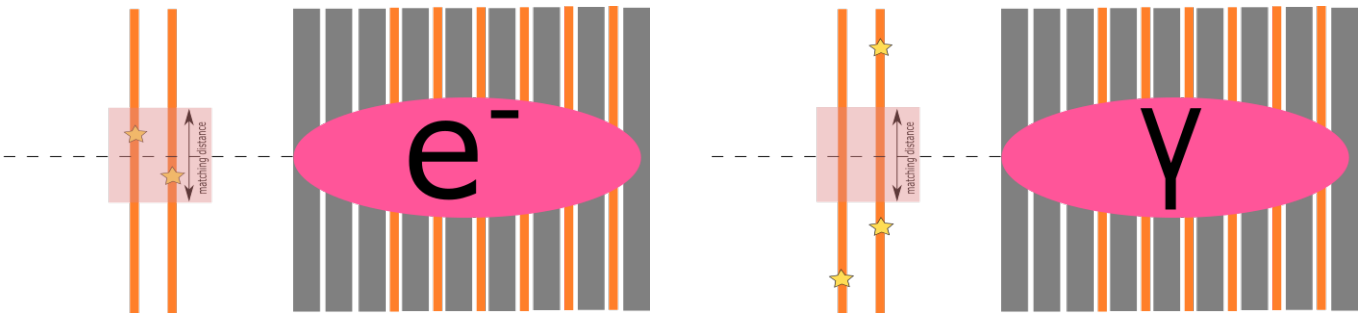

(a) (b)

Figure 2.18: (a) An example of a shower reconstructed as an electron due to the presence of hits in both sensors of the tracker at the identification distance from the shower. (b) The shower is reconstructed as a gamma quantum due to the absence of hits in both sensors of the tracker at the identification distance from the shower.

that have been reconstructed and must be reconstructed to the number reconstructed electrons (gamma rays).

Efficiency gives an estimate of how often the algorithm does not identify the particle that it should have. Correctness — how often the algorithm finds particles that did not actually exist. Ideally, we want to achieve maximum efficiency and correctness.

To assess the error of the calculated efficiency or correctness, it was assumed that particle identification can be represented as a binomial process with a certain probability of success — efficiency (correctness) [14]. Then the variation in the number of successful events" — $Var(k) = npq = n\epsilon(1-\epsilon)$.

From this we can get that the error of the values, calculated as the ratio $\frac{k}{N}$, can be written as:

$$\delta\epsilon = \frac{k}{N}\sqrt{\frac{1}{k} - \frac{1}{N}} \tag{2.5}$$

In Fig. **??** shows the dependence of the efficiency and correctness of the electron identification algorithm for events with two separate clusters and excluding direct scattering. To evaluate the efficiency and correctness, we choose a certain optimal identification distance for which the efficiency and correctness are quite large and the distance value is small. This is necessary so that the algorithm can be applied to drains close to each other. In Fig. **??** shows the sum of efficiency and correctness for Monte Carlo with and without backscattering events. The optimal identification distance — 3 mm" was selected to obtain the final values.

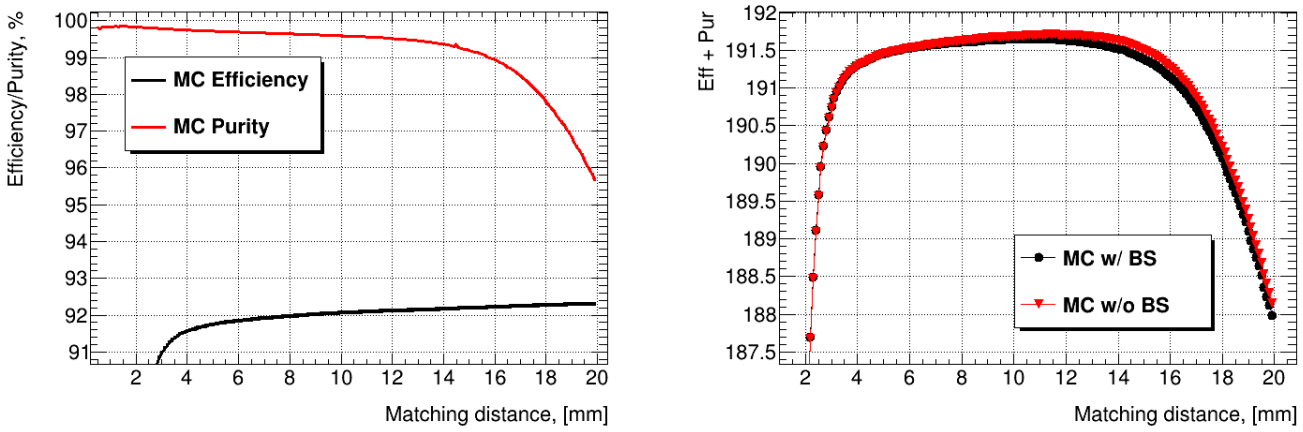

(a) (b)

Figure 2.19: (a) Dependence of the efficiency and correctness of the electron identification algorithm depending on the identification distance. (b) Dependence of the sum of efficiency and correctness on the identification distance.

The results of efficiency and correctness for the identification distance of 3 mm for the electron identification algorithm are listed in table. 3. The presence of backscattering does not affect the efficiency and accuracy of electron identification.

Electron identification		
	Efficiency, %	Correctness, %
Monte Carlo	90.966 ± 0.018	99.803 ± 0.003
Monte Carlo without backscattering	90.941 ± 0.018	99.813 ± 0.003
The difference	0.026 ± 0.018	-0.01 ± 0.003

Table 3: Efficiency and correctness of the electron identification algorithm with and without backscattering.

Fig. 2.20a shows the efficiency and correctness of the gamma-ray identification algorithm depending on the identification distance. Unlike graphs for an electron, as the identification distance increases, the efficiency decreases and the accuracy increases. From Fig. **??** it can be seen that the graphs of the sum for Monte Carlo with and without backscattering differ. The optimal identification distance of 3 mm was selected.

The efficiency, accuracy, and effect of backscattering on gamma quantum identification are shown in Table 4. Backscattering does not affect the correctness of the algorithm,

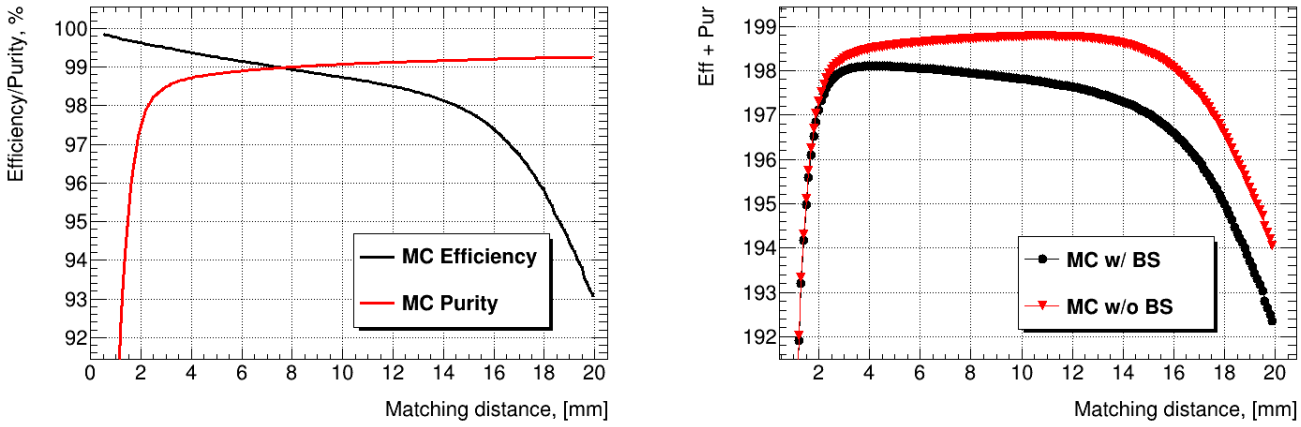

(a) (b)

Figure 2.20: (a) Dependence of efficiency and correctness of gamma quantum identification algorithm depending on hit identification distance. (b) Dependence of the sum of efficiency and correctness on the identification distance.

but reduces the efficiency of identification of gamma quants on

Gamma ray identification		
	Efficiency, %	Correctness, %
Monte Carlo	99.506 ± 0.004	98.504 ± 0.008
Monte Carlo without backscattering	99.806 ± 0.003	98.501 ± 0.008
The difference	-0.3 ± 0.004	0.002 ± 0.008

Table 4: Efficiency and correctness of the gamma-ray identification algorithm with and without backscattering.

3 LumiCal testing in March 2020

In March 2020, another test of the LumiCal detector prototype was performed on the DESY-II accelerator. Compared to testing in 2016, a number of improvements were made:

A more modern pixel telescope ALPIDE [15; 16] was used. It consists of 512×1024 pixels with a spatial resolution of 5 micrometers and a recording efficiency of over 99 %. ALPIDE telescope sensors are shown in Fig. 3.1. In the experiment, the LumiCal detector was placed closer to the telescope than in 2016 to use track position information in data analysis.

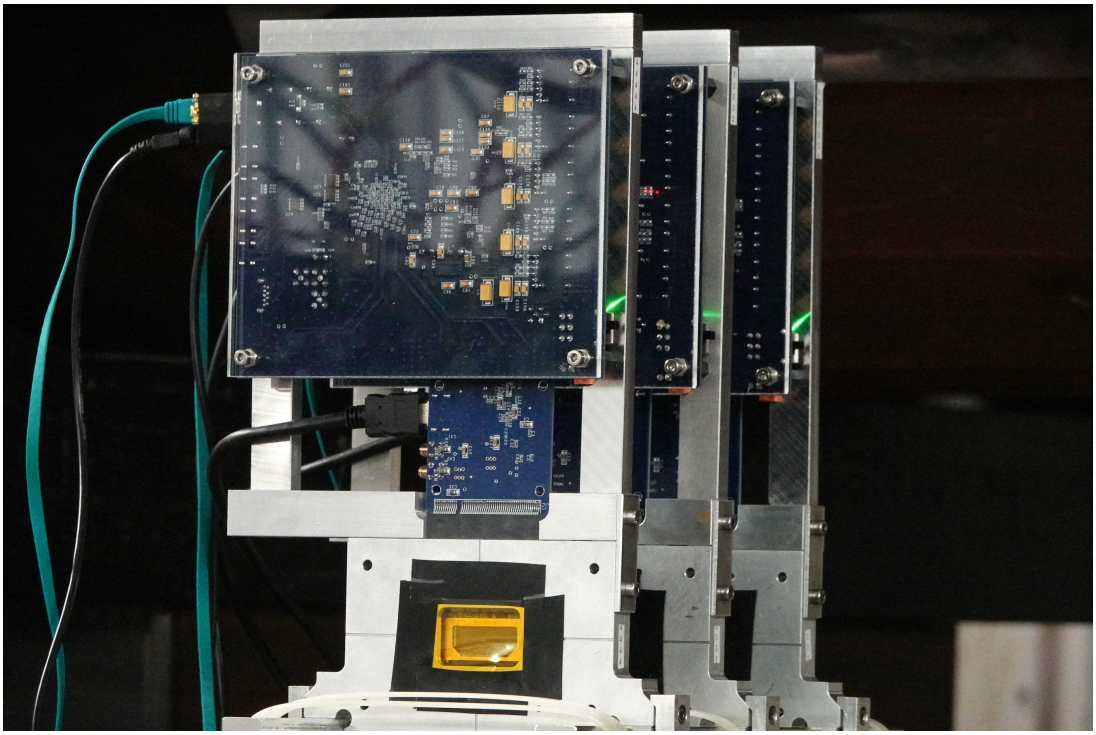

Figure 3.1: Three pixel sensors of the new ALPIDE telescope.

8 more sensors for LumiCal calorimeter were made. It now consisted of 16 layers of sensor-absorbers, which is 80 % of its planned length for ILD. This allows you to measure the Moliere radius of the calorimeter and analyze the propagation of the shower at full absorption.

The APV-25 reading electronics used in the 2016 test were designed for CMS (Compact Muon Solenoid) track detectors and are not very suitable for reading signals from a calorimeter. It served as a temporary replacement in testing in 2016, while the reading electronics for the LumiCal FLAME calorimeter (FcaL Asic for Multiplane rEadout) were in development [**Idzik: 2016xpn**; 17].

At the time of testing in March 2020, three FLAME readers were manufactured. They

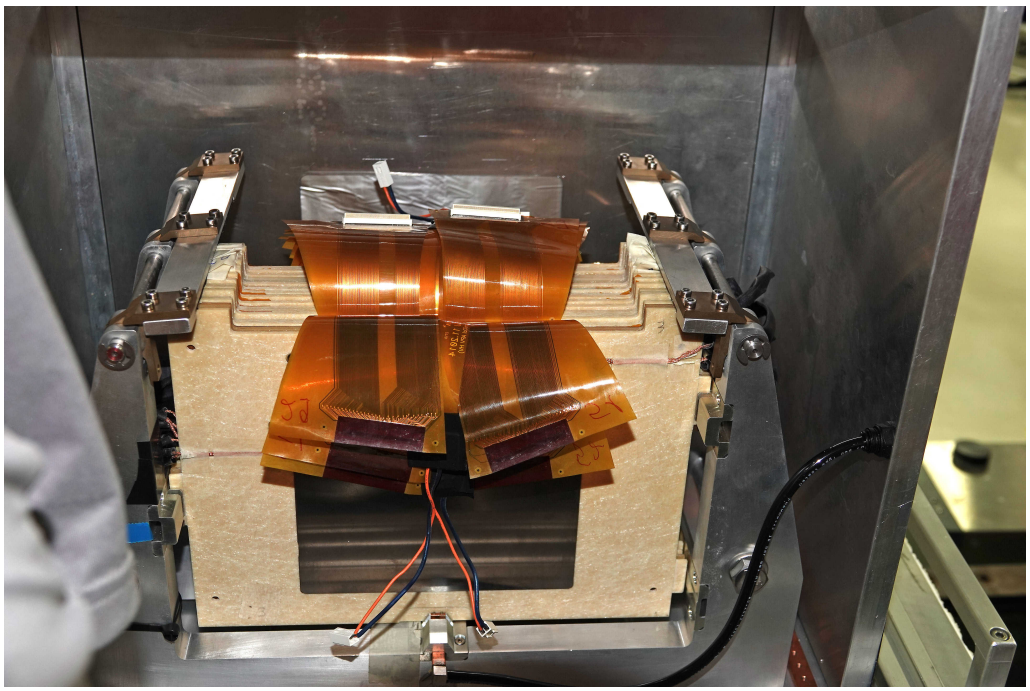

Figure 3.2: LumiCal detector in a special box. Fanout outputs from sensors for connection of reading electronics hang from above.

were connected to the first three LumiCal calorimeter sensors to record rainwater propagation data and test new electronics.

Compared to the APV-25, the recording speed of FLAME events is ten times higher and was limited by the recording speed of the ALPIDE telescope. FLAME also had the ability to record the trigger number when the system that works with APV-25 reading electronics does not have this capability, which leads to difficulties in synchronization.

Schematically, the geometry of the experiment is shown in Fig. 3.4. An electron beam with an energy of 1-6 GeV passes through a square collimator measuring 5×5 mm, 2 scintillators operating in a matching circuit as a trigger, and 5 pixel plates of the ALPIDE telescope. The electrons then enter the LumiCal calorimeter.

Several types of measurements were planned for testing:

1. **FLAME check**: Three FLAME readers connected in turn to all 16 sensors to check the FLAME's operation with each of the sensors and to investigate the distribution of rainfall along the entire length of the calorimeter.
2. **Variation of energies**: with the connection of 8 more sensors with APV-25 in addition to FLAME, measurements were made with electrons of different energies from 1 to 6 GeV.

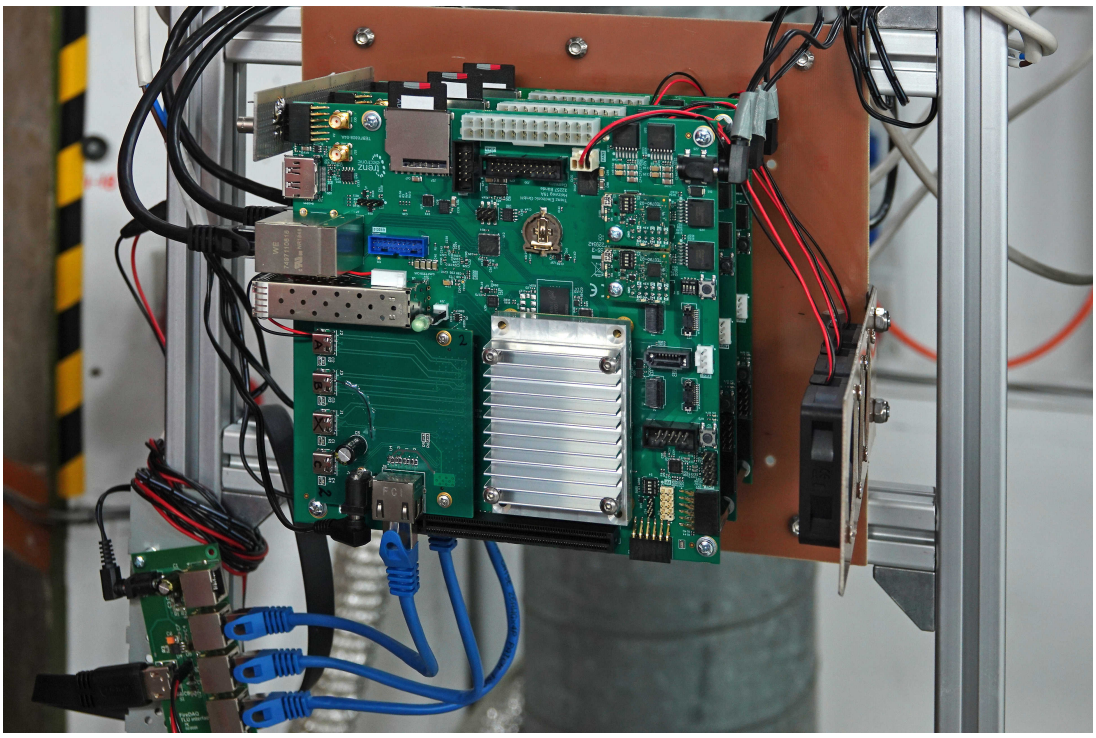

Figure 3.3: View of ASIC FLAME readers.

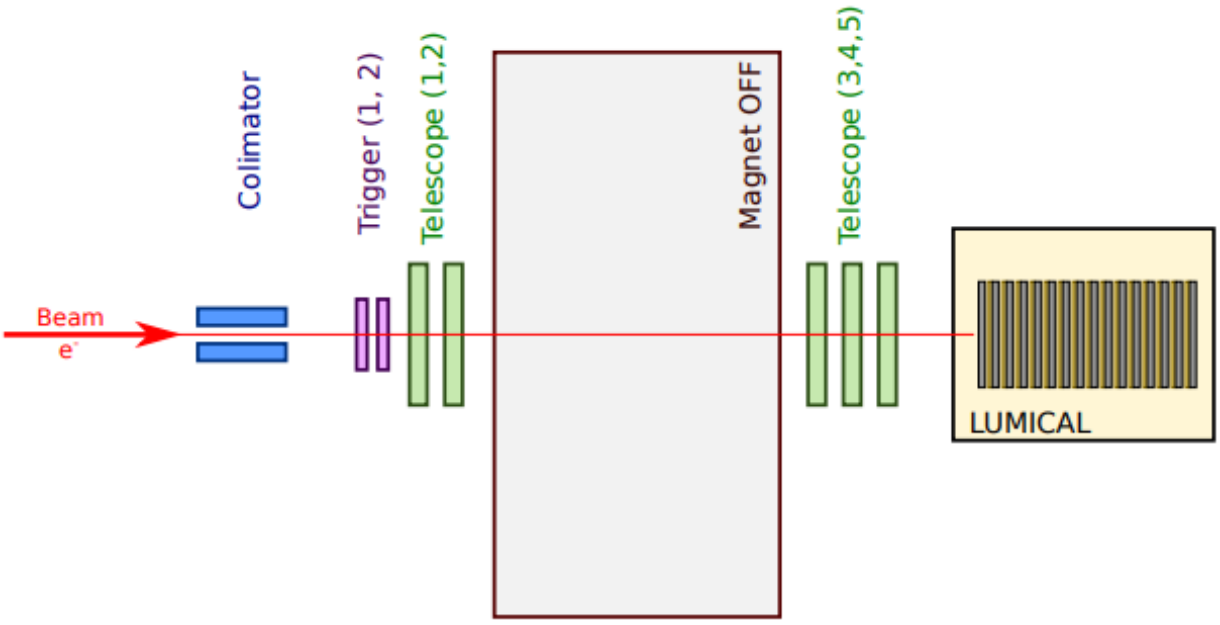

Figure 3.4: Schematic representation of the geometry of the LumiCal calorimeter test in March 2020 on the DESY-II accelerator.

3. **Inclined LumiCal**: Measure with an inclined detector at 2, 4, 6 degrees to investigate the propagation of a downpour with particles flying into the calorimeter at an angle. Test of approximate conditions to the location in ILD.
4. **Position variation**: LumiCal position gradually changed. The loss of rainwater

energy depending on the distance to the edge of the calorimeter was studied.

Now the test data has been reconstructed, is freely available and is awaiting physical analysis from the next generation of students.

Conclusions

By simulating LumiCal detector tests in Geant4, it was investigated that backscattered particles are observed as spurious signals in the LumiCal tracker used to identify particles in 2.55 % of events. These were mainly electrons (1.53 %), gamma quants (0.79 %), positrons (0.26 %) and hadrons (0.02 %), where the numbers are given for the second tracker sensor.

A particle identification algorithm was written and it was shown that backscattering had no effect on the identification of charged particles, but reduced the efficiency of neutral particle identification by 0.3 ± 0.004 %.

It can be argued that the effect of backscattering on identification is small and will not interfere with the identification of particles in the ILC project.

Development of the LumiCal detector continues and so far 16 sensors and three circuits of new reading electronics have been produced, which were tested in March 2020.

Acknowledgemtns

I want to thank my supervisors Halina Abramowicz and Aharon Levy for the tremendous support and immense experience I gained during my work.

Volodymyr Aushev, for the opportunity to cooperate with the FCAL collaboration, constant support and patience in examining the diploma.

Wolfgang Lohmann for helping through the analysis and interesting days spent in the office together.

Sima Saharof and her family for one in a life time experience and six months spent in Tel Aviv like at home. Thanks a lot for warm days. All the best for you and your family.

Karen Hernandez for an unforgettable trip to Belgium and great moral support during my visit. Thank you very much.

All participants of the LumiCal detector test in 2020. It was very interesting to meet and get to know each of you. Individual thank to colleagues from Poland, you were incredible!

To all my friends, parents and acquaintances for their support and for whom I grew up and what I was able to achieve.

Literature

1. Observation of a new particle in the search for the Standard Model Higgs boson with the ATLAS detector at the LHC / G. Aad [et al.] // Physics Letters B. — 2012. — Sept. — Vol. 716, no. 1. — P. 1–29. — ISSN 0370-2693. — DOI: 10.1016/j.physletb.2012.08.020.
2. *Troitsky S.* Unsolved problems in particle physics. — 2011. — arXiv: 1112.4515 [hep-ph].
3. The International Linear Collider: A Global Project / P. Bambade [et al.]. — 2019. — arXiv: 1903.01629 [hep-ex].
4. The International Linear Collider Technical Design Report - Volume 4: Detectors / T. Behnke [et al.]. — 2013. — arXiv: 1306.6329 [physics.ins-det].
5. Forward instrumentation for ILC detectors / H. Abramowicz [et al.] // Journal of Instrumentation. — 2010. — Dec. — Vol. 5, no. 12. — P12002–P12002. — ISSN 1748-0221. — DOI: 10.1088/1748-0221/5/12/p12002.
6. Precision luminosity measurement at ILC / I. Bozovic-Jelisavcic [et al.]. — 2014. — arXiv: 1403.7348 [physics.acc-ph].
7. The DESY II test beam facility / R. Diener [et al.] // Nuclear Instruments and Methods in Physics Research Section A: Accelerators, Spectrometers, Detectors and Associated Equipment. — 2019. — Apr. — Vol. 922. — P. 265–286. — ISSN 0168-9002. — DOI: 10.1016/j.nima.2018.11.133.
8. Performance and Molière radius measurements using a compact prototype of LumiCal in an electron test beam / H. Abramowicz [et al.] // The European Physical Journal C. — 2019. — July. — Vol. 79, no. 7. — ISSN 1434-6052. — DOI: 10.1140/epjc/s10052-019-7077-9.
9. Geant4—a simulation toolkit / S. Agostinelli [et al.] // Nuclear Instruments and Methods in Physics Research Section A: Accelerators, Spectrometers, Detectors and

Associated Equipment. — 2003. — Vol. 506, no. 3. — P. 250–303. — ISSN 0168-9002. — DOI: https://doi.org/10.1016/S0168-9002(03)01368-8.

10. Recent developments in Geant4 / J. Allison [et al.] // Nuclear Instruments and Methods in Physics Research Section A: Accelerators, Spectrometers, Detectors and Associated Equipment. — 2016. — Vol. 835. — P. 186–225. — ISSN 0168-9002. — DOI: https://doi.org/10.1016/j.nima.2016.06.125.

11. Geant4 developments and applications / J. Allison [et al.] // IEEE Transactions on Nuclear Science. — 2006. — Vol. 53, no. 1. — P. 270–278.

12. *Brun R.*, *Rademakers F.* ROOT — An object oriented data analysis framework // Nuclear Instruments and Methods in Physics Research Section A: Accelerators, Spectrometers, Detectors and Associated Equipment. — 1997. — Vol. 389, no. 1. — P. 81–86. — ISSN 0168-9002. — DOI: https://doi.org/10.1016/S0168-9002(97)00048-X. — New Computing Techniques in Physics Research V.

13. Design and results from the APV25, a deep sub-micron CMOS front-end chip for the CMS tracker / M. French [et al.] // Nucl. Instrum. Meth. A. — 2001. — Vol. 466. — P. 359–365. — DOI: 10.1016/S0168-9002(01)00589-7.

14. *Paterno M.* Calculating efficiencies and their uncertainties. — 2004. — Dec. — DOI: 10.2172/15017262.

15. EUDAQ—a data acquisition software framework for common beam telescopes / P. Ahlburg [et al.] // Journal of Instrumentation. — 2020. — Jan. — Vol. 15, no. 01. — P01038–P01038. — DOI: 10.1088/1748-0221/15/01/p01038.

16. *Rinella] G. [* The ALPIDE pixel sensor chip for the upgrade of the ALICE Inner Tracking System // Nuclear Instruments and Methods in Physics Research Section A: Accelerators, Spectrometers, Detectors and Associated Equipment. — 2017. — Vol. 845. — P. 583–587. — ISSN 0168-9002. — DOI: https://doi.org/10.1016/j.nima.2016.05.016. — Proceedings of the Vienna Conference on Instrumentation 2016.

17. *Ghenescu V.* R&D with very forward detectors at linear colliders // Nuclear and Particle Physics Proceedings. — 2016. — Vol. 273–275. — P. 2545–2547. — ISSN 2405-6014. — DOI: https://doi.org/10.1016/j.nuclphysbps.2015.09.454. — 37th International Conference on High Energy Physics (ICHEP).